PHYSICAL REVIEW C **81**, 035503 (2010)

Radiative β decay of the free neutron

R. L. Cooper and T. E. Chupp
University of Michigan, Ann Arbor, Michigan 48109, USA

M. S. Dewey, T. R. Gentile, H. P. Mumm, J. S. Nico, and A. K. Thompson
National Institute of Standards and Technology, Gaithersburg, Maryland 20899, USA

B. M. Fisher, I. Kremsky, and F. E. Wietfeldt
Tulane University, New Orleans, Louisiana 70118, USA

E. J. Beise and K. G. Kiriluk
University of Maryland, College Park, Maryland 20742, USA

J. Byrne
University of Sussex, Brighton, BN1 9QH, United Kingdom

K. J. Coakley
National Institute of Standards and Technology, Boulder, Colorado 80305, USA

C. Fu
Indiana University, Bloomington, Indiana 47408, USA

(Received 5 October 2009; revised manuscript received 5 February 2010; published 24 March 2010)

The theory of quantum electrodynamics predicts that the β decay of the neutron into a proton, electron, and antineutrino is accompanied by a continuous spectrum of emitted photons described as inner bremsstrahlung. While this phenomenon has been observed in nuclear β decay and electron-capture decay for many years, it has only been recently observed in free-neutron decay. We present a detailed discussion of an experiment in which the radiative decay mode of the free neutron was observed. In this experiment, the branching ratio for this rare decay was determined by recording photons that were correlated with both the electron and proton emitted in neutron decay. We determined the branching ratio for photons with energy between 15 and 340 keV to be $(3.09 \pm 0.32) \times 10^{-3}$ (68% level of confidence), where the uncertainty is dominated by systematic effects. This value for the branching ratio is consistent with theoretical predictions. The characteristic energy spectrum of the radiated photons, which differs from the uncorrelated background spectrum, is also consistent with the theoretical spectrum.

DOI: 10.1103/PhysRevC.81.035503 PACS number(s): 23.40.−s, 14.20.Dh, 29.40.Mc

I. INTRODUCTION

Quantum electrodynamics (QED) predicts that the β decay of the neutron into a proton, electron, and antineutrino is accompanied by the emission of inner-bremsstrahlung photons. While inner-bremsstrahlung photons have been measured in nuclear β decay and electron-capture decays, only recently has radiative β decay been measured in the neutron. In 2002, an experiment placed a limit on the branching ratio for photons with energies of 35–100 keV at 6.9×10^{-3} [1]. We subsequently reported the observation of neutron radiative β decay and determined the branching ratio for photons with energies between 15 and 340 keV [2]. In this paper, we present a detailed description of the design, operation, and analysis of this experiment, and we update the branching ratio for photons with energies between 15 and 340 keV to be $(3.09 \pm 0.32) \times 10^{-3}$ (68% level of confidence).

The photon energy spectrum and branching ratio in neutron radiative decay was first calculated analytically within a QED framework by Gaponov and Khafizov [3–5]. Glück had previously calculated this numerically in connection with radiative corrections within baryon decay [6]. Bernard *et al.* subsequently calculated the photon energy spectrum and photon polarization in neutron decay using heavy baryon chiral perturbation theory (HBχPT) including explicit Δ degrees of freedom [7,8]. The QED calculation treats the nucleons as point-like, whereas HBχPT includes the effect of nucleon structure in a systematic way. The HBχPT calculation includes all terms which are reduced by approximately m_e/M, where m_e is the electron mass and M is the nucleon mass. These additional terms contribute less than 0.5%, and both the photon energy spectrum and the photon polarization observables are dominated by electron inner bremsstrahlung.

The topics addressed in this paper are outlined here. In Sec. II, we summarize the basic theory to understand how this decay branch relates to the radiative corrections affecting the neutron lifetime. In Sec. III, we review the experimental apparatus and data collection scheme. In Sec. IV, we discuss the analysis procedure and the Monte Carlo methods and their

validation. In Sec. V, we discuss the systematic corrections and uncertainties reported for the branching ratio. Finally, in Sec. VI, we summarize the final extraction of the branching ratio and describe work under way to improve the measurement of the branching ratio and the photon energy spectrum.

II. THEORETICAL DEVELOPMENT

The neutron is composed of two down quarks and an up quark and is stable under strong and electromagnetic interactions. The weak interaction, however, can convert a down quark into an up quark through the emission of a virtual W^- gauge boson that subsequently decays into an electron and an antineutrino. Bremsstrahlung emission is expected due to the presence of real (and virtual) particles that interact electromagnetically. Reference [9] provides a useful pedagogical discussion of electron bremsstrahlung from a classical electrodynamics framework. The first section below motivates radiative decay as an important contribution to the radiative corrections in the neutron decay lifetime. The leading radiative decay matrix element is also examined.

A. Neutron decay and radiative corrections

The lifetime of the neutron contains contributions from every possible decay branch. The inverse of the total neutron lifetime τ_n can be written as

$$\frac{\hbar}{\tau_n} = \frac{(m_e c^2)^5}{2\pi^3(\hbar c)^6}|V_{\rm ud}|^2 G_F^2(1+3\lambda^2)(1+C_{\rm RC})f, \qquad (1)$$

where $\hbar$ is Planck's constant divided by 2π, m_e is the electron mass, and c is the speed of light [10]. Neutron decay is normalized to the total muon decay rate through the Fermi coupling constant [11]

$$G_F/(\hbar c)^3 = (1.16637 \pm 0.00001) \times 10^{-5}\ {\rm GeV}^2. \qquad (2)$$

Any corrections common to neutron and muon decay are factored into G_F [12]. $V_{\rm ud}$ is the element of the Cabibbo-Kobayashi-Maskawa matrix linking the up quark to the down quark through electroweak decay. The most precise value of $V_{\rm ud}$ is extracted from $0^+ \to 0^+$ super-allowed nuclear decays. The Particle Data Group value is $V_{\rm ud} = 0.97418 \pm 0.00026$ [11]. The total uncertainty is from the nuclear structure, Coulomb distortions, and uncertainties in virtual particle loop diagrams [12]. The parameter λ is the ratio of the axial-vector coupling to the vector coupling at zero momentum transfer, and it is extracted from angular and polarization correlation experiments in neutron decay. The Particle Data Group value is $\lambda = -1.2694 \pm 0.0028$ [11]. The phase-space statistical factor $f = 1.6887 \pm 0.00015$, and it includes the relatively large Fermi function contribution (~5.6%), which accounts for the Coulomb attraction of the proton and electron in the final state [10,13]. Finally, $C_{\rm RC}$ is the total contribution of all the electroweak radiative corrections where $1 + C_{\rm RC} = 1.03886 \pm 0.00039$ [13].

Radiative decay contributes to the electroweak radiative corrections $C_{\rm RC}$ through Sirlin's universal function $g(E_e)$. The radiative decay exhibits a divergence to infinity as the photon energy goes to zero. These infrared divergences are canceled by virtual photon loop contributions to neutron decay, which leaves only a small, finite contribution to $g(E_e)$. When integrating over the entire photon spectrum, this cancellation of the infrared divergence occurs at all orders of α, a well-known result from QED [14–17]. An experiment measuring the radiative decay mode is realized within a photon energy window, and an investigation of the energy dependence of this cancellation is possible.

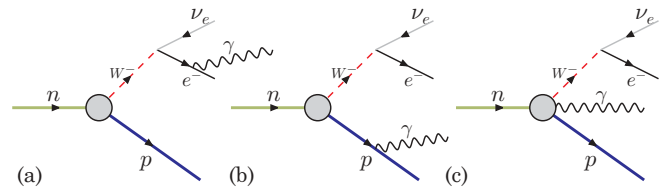

FIG. 1. (Color online) Feynman diagrams for radiative decay, (a) electron bremsstrahlung, (b) proton bremsstrahlung, and (c) bremsstrahlung from weak vertex.

B. Radiative decay matrix element and decay rate

The leading-order Feynman diagrams for a single photon radiative decay process are shown in Figs. 1(a) and 1(b). The first two diagrams are inner bremsstrahlung from the electron and proton and can be calculated with QED [3–5]. The QED matrix element for an unpolarized neutron decay is

$$\begin{aligned}\mathcal{M} = i\frac{eg_V}{\sqrt{2}}\Bigg[&\bar{u}_e(p_e)\frac{(2p_e\cdot\epsilon + \not{\epsilon}\not{k})}{2p_e\cdot k}\gamma_\mu(1-\gamma_5)v_\nu(p_\nu)\\ &\times \bar{u}_p(p_p)\gamma^\mu(1+\lambda\gamma_5)u_n(p_n)\\ &-\bar{u}_e(p_e)\gamma_\mu(1-\gamma_5)v_\nu(p_\nu)\\ &\times \bar{u}_p(p_p)\frac{(2p_p\cdot\epsilon + \not{\epsilon}\not{k})}{2p_p\cdot k}\gamma^\mu(1+\lambda\gamma_5)u_n(p_n)\Bigg], \qquad (3)\end{aligned}$$

where e is the electron charge. The parameter g_V is the vector coupling constant and by comparing to Eq. (1), it can be defined as $g_V^2 = (1 + C_{\rm RC})|V_{\rm ud}|^2$. The u and v are the spinors for the neutron, proton, electron, and antineutrino. The four-momenta for the neutron, proton, electron, antineutrino, and photon are p_n, p_p, p_e, p_ν, and k. The Dirac matrices are γ_μ and γ_5. The four-vector dot product between four-vectors a and b is $a \cdot b$ while $\not{a} = a^\mu\gamma_\mu$. The photon polarization four-vector is ϵ, and it is transverse to the photon momentum. Because the polarization of a real photon (not virtual) does not have a timelike polarization component, its four-vector dot product with the photon momentum equals the three-vector dot product $k \cdot \epsilon = \boldsymbol{k} \cdot \boldsymbol{\epsilon} = 0$. Here, the spacelike components of the photon polarization and momentum are $\boldsymbol{\epsilon}$ and $\boldsymbol{k}$ which are transverse to each other. The first and second terms in Eq. (3) (first two and last two lines, respectively) are the amplitudes for the electron and proton to couple to the outgoing photon, respectively. The electron bremsstrahlung contribution dominates because the electron mass is much less than the proton mass.

Bremsstrahlung from the weak vertex is represented in Fig. 1(c), and its contribution is expected to be model dependent. Using HBχPT, an explicit calculation has been

performed by Bernard *et al.* [7,8]. This calculation included terms occurring at next to leading order ($\sim m_e/m_n$) including explicit Δ degrees of freedom. These contributions were determined to be on the order of 0.5% and subsume all contributions from recoil order terms in the electron bremsstrahlung, proton bremsstrahlung, weak vertex emission, etc. Although separation of these individual effects could not be performed in a rigorous way, Bernard *et al.* found that their effect was scarcely distinguishable from the leading-order result. No specific energy or angular dependence is explicitly stated in these works. Given the experimental precision of our result, these contributions are imperceptible.

The differential decay rate from an unpolarized neutron can be calculated from the matrix element in Eq. (3). At leading order in nucleon mass and assuming time-reversal invariance, the result is

$$\begin{aligned}\frac{d\Gamma}{dE_e d\omega d\Omega_e d\Omega_\nu d\Omega_\gamma} &= -\alpha\frac{g_V^2|\mathbf{p_e}|E_\nu\omega}{(2\pi)^7}(1+3|\lambda|^2)\Bigg[E_\nu\left(\frac{1}{\omega}+\frac{E_e}{\omega^2}\right.\\ &+\left.\frac{m_e^2(E_e+\omega)}{(p_e\cdot k)^2}-\frac{(\omega+2E_e)}{(p_e\cdot k)}-2\frac{E_e^2}{(p_e\cdot k)\omega}\right)\\ &+a\mathbf{p}_\nu\cdot\left(\frac{\mathbf{p_e}}{\omega^2}+m_e^2\frac{(\mathbf{p_e}+\mathbf{k})}{(p_e\cdot k)^2}\right.\\ &-\left.\frac{(\mathbf{p_e}+\mathbf{k})}{(p_e\cdot k)}-E_e\frac{(\mathbf{p_e}+2\mathbf{k})}{(p_e\cdot k)\omega}\right)\Bigg],\end{aligned} \tag{4}$$

where E_i is the energy for species i, $\mathbf{p_i}$ is the three-momentum of species i, ω is the photon energy, and $\mathbf{k}$ is the three-momentum of the photon ($\omega = |\mathbf{k}|$). The parameter $a = (1-|\lambda|^2)/(1+3|\lambda|^2)$, and $\alpha \approx 1/137$ is the fine structure constant. With the approximation that $p_p \cdot k \approx m_p\omega$, where m_p is the proton mass, this result agrees with the differential decay rate from previous calculations [3,7,8].

III. EXPERIMENTAL METHOD AND APPARATUS

To observe the photons from the radiative decay mode, an experiment was undertaken to measure the decay electron, proton, and photon in coincidence. The experiment commenced in January of 2004 and operated until November of 2005 at the National Institute of Standards and Technology (NIST) Center for Neutron Research (NCNR) in Gaithersburg, Maryland. The primary experimental challenge in observing the radiative β decay of the neutron is to distinguish the low rate of energetic radiative decay photons from the large photon background associated with a neutron beam. The branching ratio for photons with energy above 15 keV is approximately 3×10^{-3}, and because the neutron lifetime is approximately 15 min, the production rate of detectable photons is small. To distinguish radiative decay photons from uncorrelated background photons, a measurement of the prompt electron and photon followed by the delayed proton signals was performed. To improve charged-particle collection efficiency, a large magnetic field to constrain the charged particles was utilized.

A. Neutron beamline

The experiment was mounted at the NG-6 fundamental physics endstation [18] at the NCNR. A cold neutron beam entered the beryllium-coated neutron guides and the collimation system originally designed for use in a neutron time-reversal violation experiment [19]. This system was adapted for the experiment by implementing slight changes in the beam optics. The collimation used a series of ^{6}LiF apertures backed with lead to define the beam, and the vacuum hardware was lined with ^{6}Li glass to absorb scattered neutrons, thus reducing background radiation. After traversing the detection region, the beam exited the vacuum system and was stopped with a ^{6}LiF beam stop approximately 1 m downstream. The pressure in the vacuum system was typically a few times 10^{-9} mbar, as measured near the ion pumps. The bore of the superconducting magnet, where the proton and electron transport and detection took place, was at cryogenic temperatures, and it is reasonable to assume that the pressure was significantly less. At these pressures, the loss of protons due to scattering from residual gas molecules is negligible.

B. Detector design

1. Proton and electron detection

The experimental method utilized a superconducting, solenoid magnet and charged-particle detection scheme previously applied to measure both the neutron lifetime and the electron-antineutrino angular correlation coefficient, which are described elsewhere [20–22]. The cold neutron beam enters parallel to the 4.6 T field produced by the magnet, as illustrated in Fig. 2. When a neutron decays inside the high field region, the charged decay products are confined to move in cyclotron orbits whose diameters are less than 1 mm. This confinement affects the transverse component of momentum (with respect to the magnetic field direction) of the particles, while the longitudinal component of momentum guides the particle upstream or downstream along the magnetic field line. The magnetic field falls off upstream and downstream of the decay region, causing a magnetic mirroring effect for charged particles outside the decay region.

The solenoid has a 9.5° bend in the magnetic field direction at the upstream end, which allows the decay particles to be guided out of the neutron beam and into a silicon, surface-barrier detector (SBD). The SBD is 600 mm^2 in area and

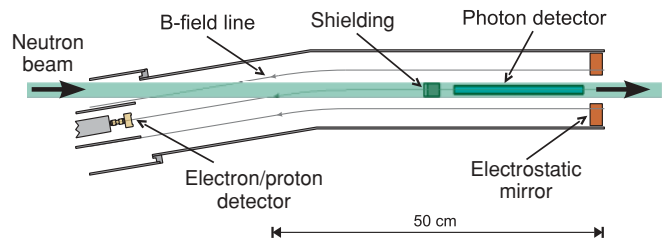

FIG. 2. (Color online) Detection scheme for measuring the radiative decay of the neutron. The shielding and detector lie below the neutron beam.

1 mm thick with a 40 μg cm^{-2} gold layer on the front face. Because the maximum proton kinetic energy is less than a keV, the SBD was biased to a potential of −25 kV to accelerate these low-energy protons through the inactive gold and silicon regions of the detector entrance window and deposit a measurable energy signal. Furthermore, the SBD and onboard preamplifier were both radiatively cooled to approximately 150 K, which improved the noise characteristics for detecting the low-energy protons. The decay electrons typically have much higher energies (several hundred keV) than the corresponding decay protons. The electrons reach the detector first, whereas the much slower protons arrive at the detector some microseconds later.

Because the protons are low energy, their trajectories can be modified by the application of modest electrostatic fields. An annular, electrostatic mirror that permitted free passage of the neutron beam was used, and it was precisely located downstream in order to reverse protons initially directed away from the SBD. Without electrostatic reflection, both particles must be emitted in the upstream direction in order to detect them. Because the electron and proton are preferentially emitted in opposite directions in a decay, electrostatic reflection increases the rate of detecting both particles together. The magnetic field in the main decay region was 4.6 T, but this field dropped to 2.6 T at the SBD, which causes the magnetic field lines to diverge as they approach the SBD. Therefore, the effective cross-sectional area for detected decay events in the central detector region is smaller than the area subtended by the SBD. A detailed study of the charged-particle trajectories in the apparatus was performed with a simulation. In these studies, the calculated electromagnetic fields are used, and they agree with measured results and those found in the previous studies using this apparatus.

2. *Photon detection*

The environment inside the bore of a superconducting magnet presented difficulties for detecting energetic photons. The high magnetic field precluded the use of a photomultiplier tube (PMT) because most PMTs are strongly affected by magnetic fields as low as 0.1 mT. To circumvent this, a pure, inorganic, scintillating crystal of bismuth germanate (BGO) was coupled to a silicon avalanche photodiode (APD). The operation of this photon detection scheme has been described in detail elsewhere [23,24].

APDs have been found to be insensitive to magnetic fields of a few tesla [25]. The signal-to-noise ratio for an APD is typically worse than that of a PMT, but both a dramatic decrease in noise and an increase in gain were observed as the temperature decreased [26,27]. At room temperature, the detection threshold was approximately 600 keV, and upon cooling, the threshold decreased by a factor of approximately 50. BGO also exhibits increased light output (a factor of approximately 3) as the temperature is lowered [28,29], which also reduced the low-energy detection threshold. The BGO fluorescence time increases to a few microseconds as the temperature is lowered, making fast timing resolution more difficult. This phenomenon arises from a spin-forbidden process responsible for light emission from the scintillator excitation [30]. Finally, photons at the energies of interest interact with BGO primarily through the photoelectric effect, with Compton scattering becoming more important at higher photon energies.

A 1.2 × 1.2 × 20 cm^3 BGO crystal [31,32] was mounted in an aluminum holder and precisely located below the neutron beam in the downstream end of the solenoid bore. A 1.35 × 1.35 cm^2 active area APD [33] was placed in direct contact with the BGO and operated with a bias of 1378 V. This is approximately 20 V below the breakdown voltage which was found to maximize the signal-to-noise ratio in the APD. An ^{241}Am source was used to calibrate the energy scale, and the photon energy detection threshold was found to be slightly below 15 keV. The threshold was set to 15 keV because events at this energy were above all the sources of noise during the calibration of the detector (both during the experimental running and in offline tests). The 60 keV peak from ^{241}Am had a 22 keV full-width at half-maximum (FWHM), and this width was dominated by the statistics of the electron-hole pair generation and multiplication in the APD [34]. The APD was connected to a preamplifier [35], and the waveforms were recorded by a digitizing card [36].

Over the course of several months of data acquisition, the gain of the photon detector was found to be stable to within 10% of the average gain. The gain was monitored by a broad 160 keV backscatter peak and 511 keV pair production peak in the photon background spectrum. These background peaks result from high-energy beam-related photons. The detector response to the ^{241}Am source and beam features are shown in Fig. 3. A more detailed examination of the calibration procedure as it relates to the systematic uncertainties is given in Sec. V A.

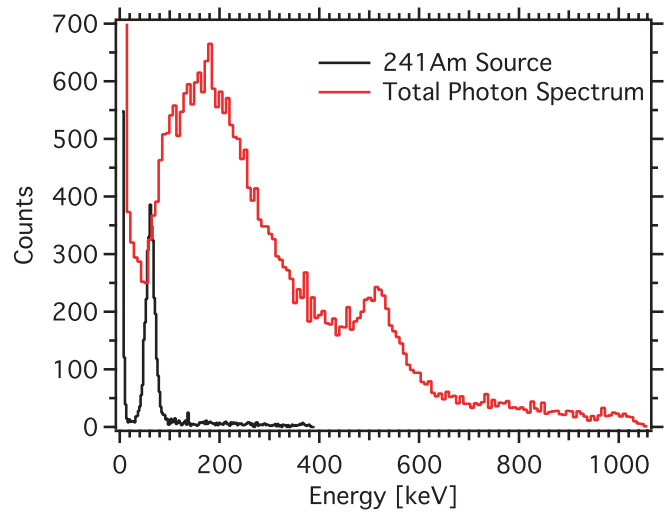

FIG. 3. (Color online) Detector response to ^{241}Am source (black) is a Gaussian peaked at 60 keV. Also shown is the total photon spectrum (gray or red) measured from a valid electron-proton trigger. The total photon spectrum contains a broad feature at 160 keV and a 511 keV pair production peak that were used as gain monitors.

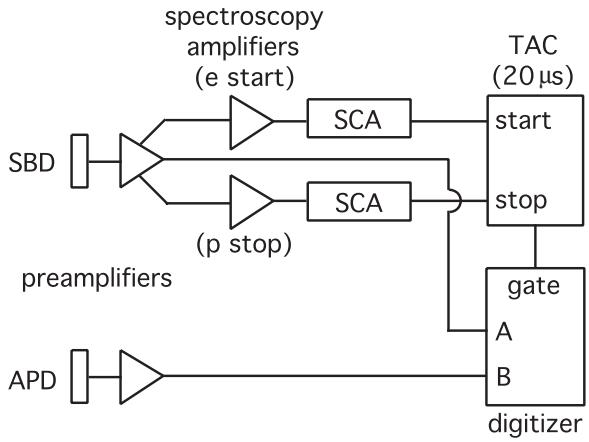

FIG. 4. Block diagram of the data acquisition system.

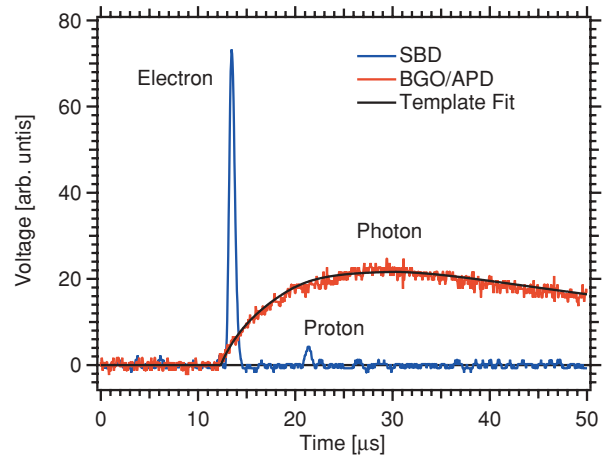

FIG. 5. Sample waveforms collected from a valid electron-proton trigger. The SBD has two shaped signal pulses for the electron and the proton (blue). The broad preamplifier pulse from the APD shows a slow rising photon signal (red). A "template fit" of the photon pulse data is also shown (black).

C. Data acquisition system

The SBD was biased to a potential of -25 kV, and its analog preamplifier signal was coupled via a fiber optic cable to the ground potential electronics. Then, it was split into two separate signals and amplified. The amplifier shaped these preamplifier signals, resulting in nearly Gaussian-shaped pulses for both the electron and proton signals. A single-channel-analyzer (SCA) window was set to encompass the entire proton pulse on one signal, and a second SCA was set on the electron pulse in the other signal. The second SCA window was set above 35 keV, which prevented a proton pulse from triggering the system. The fast timing outputs from each SCA provided the start (electron pulse) and stop (proton pulse) signals of a time-to-amplitude converter (TAC). If a proton stopped the TAC within 20 μs of an electron start pulse, a conversion signal triggered a computer-based digitizer card to record the amplified SBD signal and the preamplifier output of the APD. Figure 4 shows a block diagram of the data acquisition.

The digitizer recorded 1024 samples for each channel simultaneously at a sampling rate of 20 MHz. To examine the uncorrelated photon background, approximately 14 μs of the waveform are pretrigger data. The SBD and photon detector waveforms were recorded when a valid TAC conversion occurs; this happens regardless of the presence of a photon signal. Figure 5 shows an example of the two waveforms.

IV. DATA ANALYSIS

Events were collected in series defined as a set of consecutive runs of 10^5 events with a valid electron-proton trigger that all have the same runtime parameters (e.g., mirror voltage). A series had between 15 and 65 such runs, and they represented all valid hardware electron-proton triggers without software cuts. All of these events were stored and analyzed offline.

The purpose of the analysis was to identify all correlated electron-proton-photon (prompt electron, prompt photon, delayed proton) events from the set of data acquisition triggers. Valid decay events must also be separated from background events that can trigger the data acquisition system but do not meet the criteria of a prompt electron followed by a delayed proton. The existence of the photon does not affect the data acquisition trigger, and the photon channel is analyzed in software. Figure 4 shows a block diagram of the data acquisition. Careful extraction of the timing and energy of all the particles is crucial to identifying the correlated electron-proton-photon events. To understand the efficiency for particle detection versus the free parameter of electrostatic mirror voltage, a Monte Carlo procedure was used.

A. Data reduction

Every stored waveform was corrected in the analysis (software) for the small baseline offset that can occur. From the SBD waveform data, the energies and the difference in arrival times of the electron and proton were extracted. A window around the prompt location was analyzed to obtain the pulse height and location in time. The electron energy was estimated by integrating a ± 1.2 μs window around the peak location. If there was a photon signal in the photon detector (the criteria are discussed in the next paragraph), the electron pulse was fitted to a function that was a Gaussian convoluted with an exponential tail to refine the determination of the electron timing and energy. This function is an asymmetric Gaussian which accounts for the deviation from a true Gaussian in the electron pulse. The fit parameters are two width parameters, an overall scaling factor, and a timing offset [37]. The offset and amplitude of the fit correspond to the timing and energy of the electron, respectively. The accelerated proton was identified by the peak in the waveform occurring after the electron pulse. Its energy was found by integrating a ± 0.75 μs window around the proton pulse peak location. For those electron pulses that were not fitted (i.e., a photon was not present in the photon signal), a slewing correction was made which improved the timing extracted from the electron signal.

The presence of a photon signal is inferred from an increase in signal voltage with respect to time because of the long preamplifier tail pulse (fall time is approximately 50 μs). The timing and energy of the photon were found

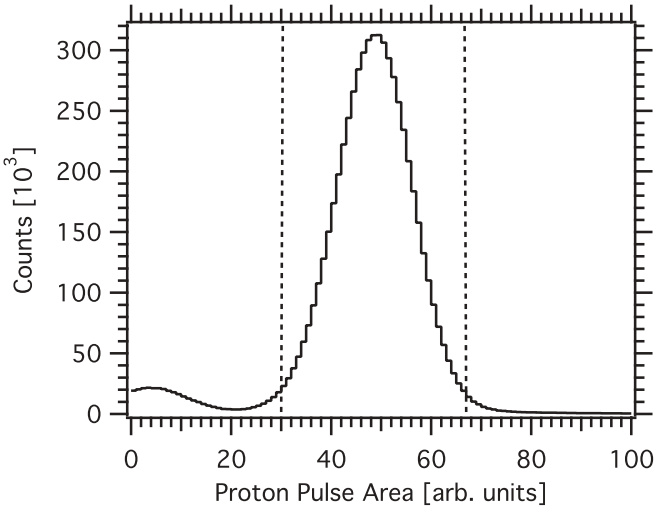

FIG. 6. Histogram of the integrated proton pulse area from valid electron-proton trigger events. The spectrum width was dominated by detector noise.

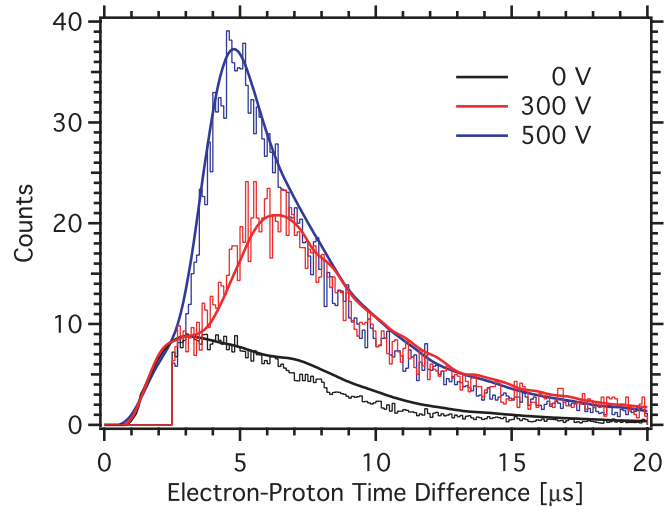

FIG. 8. (Color online) Histograms of the electron-proton time delay data in the 2.5–20 μs timing window for mirror voltages of 0, 300, and 500 V. The Monte Carlo simulation results are overlaid.

with a template fit to the waveform. The template was a model waveform constructed from the average of many photon signals that originate from the experiment and offline source tests. This template waveform was modified by three parameters representing the onset time, amplitude, and a time scaling factor. The photon pulses were then fitted by a least-squares procedure to the template function. The long fluorescence time of BGO caused the slow rise in the photon waveform (see Fig. 5), and the unshaped photon preamplifier signal was found to have better timing resolution than when shaped with an amplifier.

Several analysis cuts were made after the energy and timing for the electron, proton, and photon (if present) were determined. For the proton energy spectrum, a window corresponding to twice the FWHM of its nearly Gaussian distribution was accepted. A sample proton energy spectrum is shown in Fig. 6, and its width was dominated by detector noise. No additional electron energy cuts were made beyond the hardware threshold from the SCA. Sample electron energy spectra after all the analysis cuts and the electrostatic mirror voltage at 0 and 700 V are shown in Fig. 7. The spectrum shape is distorted from a typical β-decay electron energy spectrum, primarily due to electron backscattering. The detector response was simulated with MCNP5 [38], and it agrees with the observed spectrum shape.

Cuts were placed on the electron-proton time difference spectrum, and sample spectra for various electrostatic mirror potentials are shown in Fig. 8. Events falling within a 2.5–20 μs timing window were accepted for further analysis. The lower limit was chosen to eliminate the influence of high-energy backgrounds with long tails. Typically, such events were due to beam-related γ rays and comprised up to 10% of

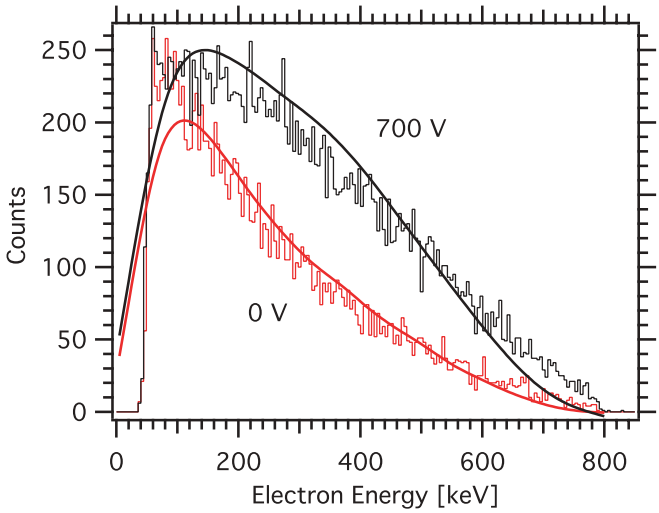

FIG. 7. (Color online) Histograms of the calibrated electron energy spectrum after application of all the analysis cuts for electrostatic mirror voltages of 0 and 700 V. The MCNP5 Monte Carlo simulation of the SBD response is overlaid.

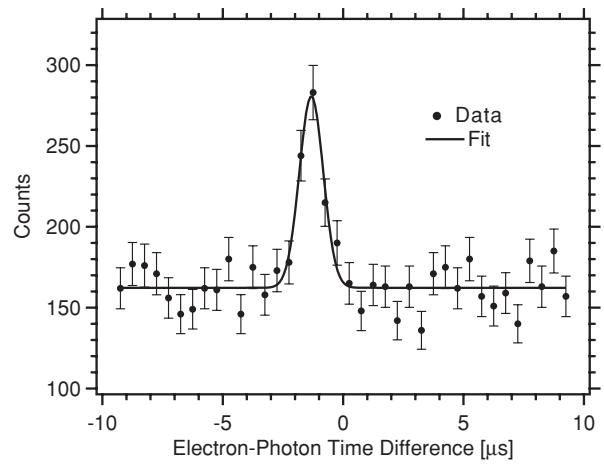

FIG. 9. Electron-photon timing spectrum for a three-day run. The spectrum shows all photons in a ± 10 μs window around the electron start pulse which was accompanied by a delayed proton event. The fitted Gaussian has a width of approximately 1 μs.

TABLE I. Cuts implemented on the data set.

Cut	Range
Proton energy	2 FWHM
Electron energy	$\geqslant$35 keV (SCA)
Photon energy	15–340 keV
e-p timing	2.5–20 μs
e-γ timing	$\geqslant$2 FWHM
e-p baseline cut	Waveform returns to baseline

the electron-proton trigger rate prior to the cut. These events were also rejected by requiring the tail of the electron pulse to return to its baseline level before the onset of the delayed proton pulse.

A time-difference spectrum was also constructed for photons that occur within a ± 10 μs window of an electron with a valid proton pulse. An electron-photon timing spectrum for a three-day run is shown in Fig. 9. Correlated photon events, including those attributable to radiative decay photons, were centered at $\Delta t = -1.25$ μs due to electronic delays. The width was approximately 1 μs, which is dominated by uncertainties in extracting the photon timing due to the APD noise. Uncorrelated electron-photon events comprised a uniform background in the electron-photon time difference spectrum, which is consistent with calculations based on the observed photon rates. After background subtraction, a window that was twice the FWHM around the electron-photon timing peak was accepted for further analysis. A summary of the cuts is given in Table I.

B. $R_{ep\gamma}/R_{ep}$ ratio extraction

By normalizing the electron-proton-photon event rate, $R_{ep\gamma}$, to the electron-proton event rate, R_{ep}, the detection efficiency of the SBD is largely canceled. The total number of electron-proton-photon events was extracted from the electron-photon timing peak (e.g., Fig. 9) after the application of the analysis cuts. The number of correlated and background events was extracted with a Gaussian plus constant background fit. The $R_{ep\gamma}/R_{ep}$ ratio was determined by a weighted average at each electrostatic mirror voltage; all the data above 700 V were averaged to a single data point plotted at 750 V. This result is shown in Fig. 10.

The extraction of electron-proton-photon events is subject to an error due to correlated background events. However, these background events were a small contribution to $R_{ep\gamma}$, and their effect is summarized in Sec. V D. The χ^2 of the ratio $R_{ep\gamma}/R_{ep}$ around the weighted average for each series was calculated at each voltage. These χ^2 values for each voltage are acceptable, even though most runs were separated by periods of many weeks.

As the mirror voltage was increased, $R_{ep\gamma}$ and R_{ep} both increased due to the reflection of more protons that are antiparallel to the electrons detected in the upstream direction. However, the $R_{ep\gamma}/R_{ep}$ ratio is also expected to increase. At low mirror voltage, the detected electron and proton tend to be correlated in the emission direction because the mirror cannot reflect the antiparallel protons. The antineutrino and

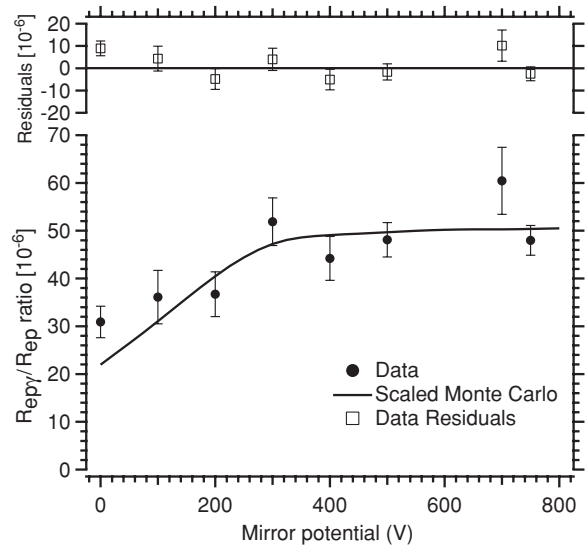

FIG. 10. Plot of the ratio of the electron-proton-photon event rate (background subtracted) to the electron-proton event rate versus the mirror voltage. The Monte Carlo calculation which was fitted to the data is overlaid. All data above 700 V were averaged into a single data point at 750 V.

photon are kinematically required to be emitted in the opposite hemisphere in order to conserve momentum. Therefore, as the mirror voltage increases, the detected proton can now be anticorrelated to the electron, helping to conserve momentum. This frees the photon from kinematic constraint. Furthermore, the dynamics of QED indicates that the decay rate is maximal when the emitted photon and electron are separated in angle by 55° when examined with uniform angular bins (the peak occurs at 35° when the bins are weighted by $\sin\theta$ which ensures uniform solid angle coverage per bin). Therefore, at lower voltages there is also a dynamic suppression that does not occur at higher voltages because the photon is no longer constrained to be emitted opposite to the electron.

The $R_{ep\gamma}/R_{ep}$ ratio data versus electrostatic mirror voltage was compared to a Monte Carlo calculation of the radiative decay spectrum in the detector, which is described in Sec. IV C. If the peak in the electron-photon timing spectrum were due to a uniform background, the expected ratio in Fig. 10 would be flat. Assuming this hypothesis and performing a weighted average of the ratio over all the potentials, the χ^2 per degree-of-freedom was 22.4/7, corresponding to a probability of 0.2%. When the Monte Carlo generated ratio was assumed and the same χ^2 procedure was performed, the χ^2 was 12.9/7 per degree of freedom, corresponding to a probability of 7.5%. This suggests that the Monte Carlo generated ratio is more consistent with the data than the uniform, correlated background hypothesis. The data analysis parameters are calculated in Table II for each series.

The photon energy spectrum of correlated events from 15 to 340 keV was determined by subtracting the photon energy spectrum in the uniform background (off-peak) from the events under the electron-photon timing peak (on-peak). The on-peak spectrum was obtained by taking a ± 1 μs window centered around peak location, while the off-peak background spectrum

TABLE II. Characterization of the 23 data series used in the experiment. V_{Mirror} is the voltage applied to the electrostatic mirror; the live time is reported in total days; e^- threshold is the measured electron threshold in keV for the series; $\langle R_{ep} \rangle$ is the average rate of valid electron-delayed proton triggers; $\langle R_\gamma \rangle$ is the average rate of photon events that have a valid electron-delayed proton trigger within a 51 μs window; $\langle R_{ep\gamma} \rangle$ is the average rate of photon events in the electron-photon timing window with a valid electron-delayed proton trigger after background subtraction (the rate of events in the peak of Fig. 9). The ratio $R_{ep\gamma}/R_{ep}$ is reported in the last column, and those values at the same voltage were averaged together to produce the data shown in Fig. 9. All data above 700 V were averaged to a single data point at 750 V.

Series	V_{Mirror} (V)	Live time (d)	e^- threshold (keV)	$\langle R_{ep} \rangle$ (s^{-1})	$\langle R_\gamma \rangle$ (s^{-1})	$\langle R_{ep\gamma} \rangle$ ($\times 10^{-5}$ s^{-1})	Ratio ($\times 10^{-6}$)
87	0	5.7	41	5.40	0.030	23.2 ± 4.3	42.9 ± 7.9
92	0	2.8	41	5.42	0.029	19.7 ± 5.8	36.3 ± 10.7
93	200	4.2	40	10.44	0.053	30.9 ± 6.6	29.6 ± 6.4
94	300	1.9	40	14.28	0.071	76.8 ± 12.2	53.8 ± 8.5
96	400	2.4	39	16.91	0.083	69.5 ± 11.5	41.1 ± 6.8
97	500	2.2	37	18.63	0.091	92.8 ± 13.0	49.8 ± 6.9
99	1500	3.1	36	19.92	0.103	89.1 ± 11.1	44.7 ± 5.6
103	0	5.7	39	3.85	0.015	14.9 ± 4.0	38.7 ± 10.3
104	1500	2.9	36	17.00	0.061	60.7 ± 11.5	35.7 ± 6.8
105	0	8.6	41	4.03	0.016	10.7 ± 3.1	26.6 ± 7.8
106	500	2.3	44	11.20	0.039	61.3 ± 11.0	54.8 ± 9.8
110	1600	2.8	32	21.85	0.075	113.0 ± 13.7	51.7 ± 6.3
111	500	3.0	33	20.15	0.070	95.2 ± 12.9	47.3 ± 6.4
112	0	6.9	33	5.84	0.023	15.3 ± 4.3	26.3 ± 7.3
114	0	6.5	32	6.32	0.023	14.8 ± 4.5	23.5 ± 7.0
115	500	2.3	32	21.47	0.073	94.5 ± 14.7	44.0 ± 6.8
119	200	4.1	36	11.26	0.039	51.1 ± 7.9	45.4 ± 7.0
122	100	5.8	32	8.26	0.030	28.1 ± 5.6	34.0 ± 6.7
123	1000	2.9	32	22.12	0.075	129.9 ± 13.8	58.7 ± 6.2
124	300	3.9	36	15.39	0.054	78.4 ± 9.6	50.9 ± 6.3
125	700	2.5	37	20.61	0.072	124.4 ± 14.4	60.4 ± 7.0
126	400	3.2	34	17.70	0.059	83.1 ± 11.2	46.9 ± 6.3
127	100	3.0	37	7.66	0.029	31.2 ± 7.5	40.8 ± 9.9

was extracted from an 8 μs window in both the pre-prompt and post-prompt regions. Figure 11 shows the resulting spectrum after the background has been scaled and subtracted. These data are compared the theoretical spectrum that was slightly modified for the photon detector response using a Monte Carlo calculation. The primary sources of these deviations are the escape of the bismuth x rays from the BGO crystal and Compton scattering within the crystal.

C. Monte Carlo methods

Extraction of the branching ratio required knowing the $R_{ep\gamma}/R_{ep}$ ratio as a function of mirror voltage. The evaluation of this ratio is a complicated interplay of the beam size, beam profile, electromagnetic fields, etc., and the Monte Carlo method was used to calculate it. This was compared with the experimental data to extract the branching ratio. Two independent Monte Carlo calculations were developed to generate and track simulated neutron decay events through a model of the experimental apparatus. The first method generated neutron decay events with conditionally integrated probability distributions and then used the fourth-order Runge-Kutta procedure to integrate the equations of motion for charged-particle transport in the electromagnetic fields. The

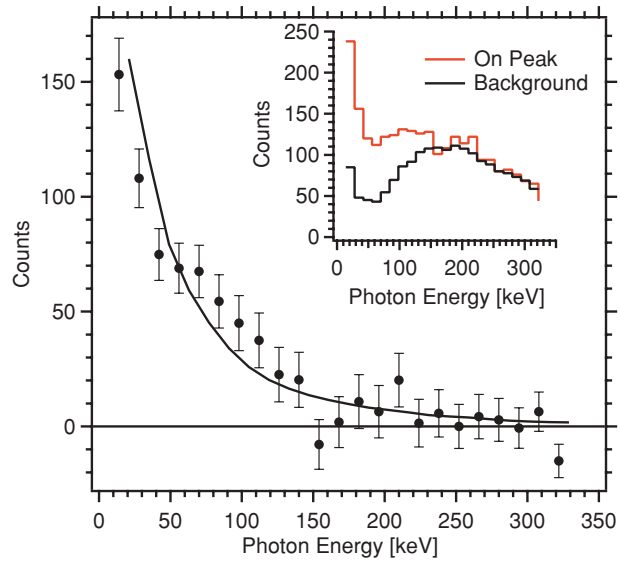

FIG. 11. Photon energy spectrum of events in the electron-photon timing peak. The inset shows the shape of the on-peak and off-peak spectra prior to the subtraction. The overlaid curve shows the spectrum calculated with the Monte Carlo that includes the effects of detector response.

second method generated events with a von Neumann rejection method and tracked the charged particles in the electromagnetic field adiabatically. Independent Monte Carlo calculations offered different insights about the experiment, and they were consistent with each other in bench-marking tests.

1. Decay generators

Two different methods of generating large numbers of realistic, simulated, neutron β-decay events were used. The probability distribution for three-body neutron β decay is derived from the results in Jackson *et al.* [39], and the probability distribution for radiative four-body neutron β decay is derived from Refs. [3,7,8] and Eq. (4). The two methods described below generate simulated neutron decay events by dealing with the multidimensional probability distributions in different ways. Overviews of Monte Carlo methods are given in Refs. [11,40].

In conditionally integrated sampling, the multidimensional probability distribution is integrated over all but one variable, say x_n. The value x_n^* is selected from the remaining one-dimensional probability distribution. In our case, von Neumann rejection was used to select x_n^* from these one-dimensional probability distribution functions. This process is repeated until all n variables have been selected conditional to the previously selected values x_i^*

$$\begin{aligned} P(x_n) &= \left(\prod_{i=1}^{n-1}\int dx_i\right) P(x_1,\ldots,x_n), \\ P(x_{n-1}|x_n^*) &= \left(\prod_{i=1}^{n-2}\int dx_i\right) P(x_1,\ldots,x_{n-1},x_n^*), \\ &\vdots \\ P(x_1|x_2^*,\ldots,x_n^*) &= P(x_1,x_2^*\ldots,x_n^*). \end{aligned} \tag{5}$$

In contrast, the von Neumann rejection method rejects events against the upper bound of the multidimensional probability distribution. Events are typically generated uniformly within the kinematically allowed parameter space; for radiative decay, the electron, photon, and antineutrino directions are each distributed uniformly into 4π solid angle, the electron energy is distributed uniformly from m_e to the endpoint energy ($\approx$1.3 MeV), and the photon energy is distributed uniformly from the lower to the upper energy limits. If the event is kinematically allowed, the probability is then calculated from the multidimensional probability distribution. The event is accepted or rejected with respect to the upper bound. The difference between the events derived from each generator was negligible.

2. Transport

The proton is nonrelativistic and has a kinetic energy less than 1 keV. The equations of motion from the nonrelativistic Lorentz force law can be solved with the fourth-order Runge-Kutta procedure. The relativistic electron can also be solved in this way, but the Lorentz force law must be modified. In the laboratory frame, it is

$$\dot{\mathbf{v}} = \frac{e}{\gamma m_e}\left[\mathbf{E} - \left(\mathbf{E}\cdot\frac{\mathbf{v}}{c}\right)\frac{\mathbf{v}}{c} + \mathbf{v}\times\mathbf{B}\right], \tag{6}$$

where $\gamma = 1/\sqrt{1-v^2/c^2}$ and v is the magnitude of the vector velocity $\mathbf{v}$. The magnetic and electric field vectors are $\mathbf{B}$ and $\mathbf{E}$, respectively. These fields are calculated and match the measured values. Because of the large magnetic field, the particles spiral in cyclotron orbits less than 1 mm in diameter. Tracking the particles through the apparatus required many small time steps to accurately trace each cyclotron orbit, and this procedure required significant computation time.

Because the magnetic field is nonzero and nearly uniform along a cyclotron orbit, the adiabatic invariant μ can be exploited. For the proton, $\mu = p_\perp(\mathbf{x})^2/2m_p B(\mathbf{x})$ where $p_\perp(\mathbf{x})$ is the magnitude of the component of momentum perpendicular to the magnetic field, m_p is the mass of the proton, and $B(\mathbf{x})$ is the magnitude of the magnetic field at position $\mathbf{x}$. Tracing the magnetic field is easily done (when the drift mechanisms are neglected), and the equations of motion are reduced to a scalar potential for the component of momentum parallel to the magnetic field $p_\parallel$. It is

$$p_\parallel^2(\mathbf{x}) = 2m_p\left[E_0 - \mu B(\mathbf{x}) - qU(\mathbf{x})\right], \tag{7}$$

where $U(\mathbf{x})$ is the electrostatic potential at position $\mathbf{x}$ and E_0 is the initial total energy. The adiabatic invariant of the relativistic electron is $\mu = p_\perp(\mathbf{x})^2c^2/B(\mathbf{x})$, where the momentum is relativistically correct [9]. The potential is

$$p_\parallel(\mathbf{x})^2c^2 = \mathcal{E}(\mathbf{x})^2 - \mu B(\mathbf{x}) - m_e^2c^4. \tag{8}$$

For an electron originating at $\mathbf{x_0}$, the energy of the particle $\mathcal{E}(\mathbf{x}) = E_0 - qU(\mathbf{x})$, where $E_0 = |\mathbf{p}(\mathbf{x_0})|^2 + m_e^2c^4 + qU(\mathbf{x_0})$ is the initial total energy. The effect of the neglected drift mechanisms can be incorporated, and they are discussed in Ref. [9].

V. SYSTEMATIC CORRECTIONS AND UNCERTAINTIES

This section describes the systematic effects that contribute to the extraction of the branching ratio. These effects are organized into five sections that relate to the photon detector, SBD calibration, analysis cuts, correlated backgrounds, and the model used in the Monte Carlo simulation. Table III summarizes the systematic corrections, systematic uncertainties, and the section where each is discussed. The corrections and uncertainties are reported as a percentage of the branching ratio. The branching ratio is extracted from a fit of the data to the Monte Carlo calculation, and the uncertainty of the fit to the experimental data is 3.4%. A more detailed treatment of the systematic effects is found in Ref. [41].

A. Photon detector uncertainties

The dominant systematic effect manifests itself in the low-energy threshold of the photon detector. The photon detector has a nonideal energy resolution and suffers from gain drifts which produce an uncertainty in the threshold value. In contrast, the Monte Carlo calculation assumed exact energy

TABLE III. Summary of the systematic effects which contribute corrections and uncertainties to the measured branching ratio. The origin of each quantity is discussed in the section indicated in the table. 0.0^* indicates that the systematic corrections are less than 0.05% in magnitude but may not be identically zero.

Source of uncertainty	Correction (%)	Uncertainty (%)	Sec.
Photon detector:			V A
Gain drift & resolution	−2.5	7.0	V A2
Photon detector efficiency	+3.0	3.0	V A3
Charged-particle energy:			V B
Electron energy threshold	0.0^*	1.5	V B2
Proton energy	0.0^*	<0.05	V B3
Timing cuts:			V C
Electron-delayed proton timing	0.0^*	2.0	V C
Electron-photon timing	0.0^*	2.0	V C
Correlated backgrounds:			V D
Electron bremsstrahlung	−3.0	3.0	V D1
Electronic artifacts	−0.5	0.5	V D2
Model uncertainties:			V E
Beam divergence/profile	0.0^*	3.0	V E1
B field registration	0.0^*	2.0	V E1
Mirror registration	0.0^*	1.0	V E1
APD bias leakage	0.0^*	1.0	V E2
Electron backscattering	+0.2	0.5	V E3
Monte Carlo statistics	0.0^*	2.0	V E
Total systematic	−2.8	9.8	
Fit uncertainty		3.4	

cuts, perfect energy resolution, and perfect detection efficiency when calculating the $R_{ep\gamma}/R_{ep}$ ratio. The nonideal detection efficiency leads to an underestimate of the number of detected photons. One example of this underestimation is a photon that does not interact in the finite length of detector that it passes through (this effect is more relevant at higher photon energies). On the other hand, the detector was surrounded by the magnet bore, which can scatter correlated photons into the detector that would not have been counted in the Monte Carlo.

The systematic effects of the photon detector can be separated into contributions affecting the detector threshold and the detector efficiency. First, the photon detector calibration (a threshold effect) is described in Sec. V A1. Systematic effects from gain drifts and detector resolution are discussed in Sec. V A2. Finally, the effect of the detector efficiency is described in Sec. V A3.

1. Photon detector calibration

The gain of the photon detector varied from series to series during experimental operation, and this affected the measured lower energy threshold. Gain shifts primarily occur because of the nonlinearity in the APD to the bias voltage and ambient temperature [27]. Given a stable temperature and bias voltage, though, the amplitude of the pulse from the APD is linearly proportional to the γ-ray energy. The photon detector energy response was calibrated *in situ* using the 60 keV line from ^{241}Am and the 511 keV line from pair production as shown in Fig. 3. The 511 keV photon was produced as a constant background from beam-related particles and served as a constant gain monitor throughout a run. A photon was recorded only when an electron-proton (prompt electron, delayed proton) trigger occurred, so approximately 1 day was required to collect enough counts to determine the calibration point. In addition to the 511 keV line, there was a broad 160 keV feature in the photon spectrum. This feature is primarily due to Compton backscattering of higher energy photons into the photon detector [42], and it was used as a gain monitor along with the 511 keV line.

The data were acquired using two photon energy windows. The runs from series 87 through 99 detected photons with energies up to approximately 800 keV. From series 103, the photon energy window was reduced to approximately 350 keV because there were no detectable radiative decay events (correlated photons) at higher energies. The smaller energy window improved the detector resolution (smaller signal range for the 8 bit digitizer), but the 511 keV line could no longer be used as a gain monitor. To use the backscattering peak as a gain monitor, the runs were summed by series to generate a photon energy spectrum. The wide backscatter peak was fitted to a Gaussian to serve as a gain monitor for each series.

2. Threshold effects

The location of the 160 keV peak used for the calibration changed by 13% over the course of running due to gain drifts; this corresponds to a ±1 keV variation around the 15 keV photon detection threshold. Because the radiative decay rate

is inversely proportional to the photon energy (ω), the effect of detector resolution is to increase the number of photons detected above threshold. The photon detector resolution was measured to be 35% at 60 keV. Assuming that the detector resolution scales as $\omega^{-1/2}$ due to the approximation of Poisson photoelectron statistics, the resolution width is approximately 10 keV at the 15 keV detection threshold.

The effect of the energy resolution at threshold was approximated by convoluting the theoretical decay spectrum with a Gaussian with a 10 keV width. This modified energy spectrum was integrated from 14 to 16 keV, which is the possible change in the position of the threshold based on the maximum drift of the calibration. The excess of photon counts required a systematic correction of -2.5% to the branching ratio, and an uncertainty of 7% was attributed to the combination of these effects. These systematic effects were also examined separately, and this analysis yielded the same systematic correction and total uncertainty.

3. Photon detector efficiency

The Monte Carlo simulations which generated the $R_{ep\gamma}/R_{ep}$ ratio did not incorporate photon detector efficiency or a model of photon scattering. The measured branching ratio tended to underestimate the theoretical branching ratio because the detection efficiency is less than unity, and it required a positive correction to the branching ratio. However, photon scattering in the apparatus tended to increase the number of detected photons, and a negative correction to the branching ratio was required. These competing effects were examined together.

MCNP5 was used to model the experimental apparatus and the BGO crystal response. It simulated the photon response of the entire apparatus to the theoretical photon energy spectrum. The result of this analysis showed that the measured branching ratio underestimated the theoretical expectation when both systematic effects were combined. A systematic correction to the branching ratio of $+3\%$ was required, and, conservatively, the size of the systematic uncertainty was set equal to the magnitude of the systematic correction.

B. Charged-particle energy

In this section, the systematic uncertainties of the charged-particle energies are examined. These energy cuts and analysis are intimately connected to the calibration of the SBD. After discussing the SBD calibration in Sec. V B1, the electron and proton energy systematic uncertainties are discussed in Secs. V B2 and V B3, respectively.

1. SBD calibration

Although the branching ratio is not highly sensitive to the electron threshold, since its effect is dominantly an efficiency that is canceled in the ratio $R_{ep\gamma}/R_{ep}$, it was still necessary to calibrate the surface barrier detector for each series. This threshold is set in the hardware by the SCA window, and the corresponding threshold energy changes as the gain of the SBD changes. Thus, the energy calibration effectively determines the threshold of the electron energy spectrum. The energy calibrations used two measured points: the 60-keV γ line from ^{241}Am and the endpoint of the β spectrum. While the measured endpoint is not exactly 782 keV due to energy loss, it provides an acceptable calibration point because the detector was sufficiently thick to absorb almost all of the β energy. An offset of zero was used because the pulses in the calibrations were analyzed as digitized waveforms, and thus the baselines for each event were subtracted.

The ^{241}Am calibrations were performed *in situ* and carried out periodically. The detector was mounted on a linear motion feedthrough that could be retracted from the magnet bore for calibration. The source was placed near the SBD but outside of the vacuum system. The vacuum system walls were sufficiently thin that the 60 keV γ rays could penetrate the walls and be detected by the SBD; the α particles from the source were absorbed. The peak of the accelerated proton energy spectrum (accelerated by a -25 kV potential) was not used as a calibration point because of energy loss in the inactive layer of the SBD, but it was used as a gain monitor.

2. Electron energy threshold

The lower energy threshold on the electron spectrum was selected in hardware with an SCA window to be above the proton peak to ensure that the data acquisition system was not triggered by the protons. Using the SBD calibration described above, the average electron threshold was easily measured for each series. The thresholds were found to vary by 12 keV around the central value of 36 keV. Table II shows the measured electron thresholds for each series. These threshold values are from the deposited electron energy in the SBD, and this spectrum is altered by the -25 kV potential on the SBD which retarded the incoming electrons.

For each series (see Table II), a correction to the $R_{ep\gamma}/R_{ep}$ ratio was calculated using the measured electron energy threshold. At each electrostatic mirror voltage, a weighted average of these corrections was made which yielded a voltage-dependent correction, and the branching ratio was extracted from this modified Monte Carlo calculation. The total systematic correction to the branching ratio was found to be less than 0.05%. The total variation of the voltage-dependent corrections was 1.5% of the branching ratio, and this value was applied as the systematic uncertainty.

3. Proton energy spectrum

The proton energy is so small that the protons were accelerated in order to be detected. When this acceleration was combined with the detector noise, the ability to extract proton energy information was eliminated. The measured proton energy spectrum is nearly a Gaussian with a FWHM of approximately 8 keV (dominated by detector noise). All events in a window twice the FWHM of the Gaussian peak were accepted, which cut approximately 2% of the protons.

The theoretical proton spectra were convoluted with a Gaussian of the same width as the experimental spectrum

to simulate the detector response. The convoluted radiative and nonradiative proton energy spectra were nearly identical but were shifted relative to each other by 0.5 eV. The systematic shift in the $R_{ep\gamma}/R_{ep}$ ratio was found to be less than 10^{-3}; therefore, it was negligible. The uncertainty was also negligible, which exhibits the power of the ratio method in ameliorating some systematic effects.

Protons can also be lost through Rutherford backscattering from the surface of the silicon on the SBD. This effect was calculated using SRIM-2006 [43], and 2% of the protons were lost. This analysis neglected the accelerating potential on the SBD, which attracted the resulting backscattered protons. This effect was the same for protons from both radiative and nonradiative decay. Thus, the systematic shift and correction had a negligible effect on the branching ratio.

C. Timing cuts

Timing cuts were made on both the electron-proton time difference and the electron-photon time difference from which the number of correlated photons were extracted. Figure 8 shows the electron-proton time difference spectrum at three values of the electrostatic mirror potential. The calibration for the timing came from the TAC, which was checked against a time calibration module. The full timing window from the TAC was 20 μs, which is known to a precision better than was needed.

The most significant contribution to the timing uncertainty was the determination of the pulse onset time from the digitized waveforms. The onset times for the electron and proton were extracted in the analysis, and after the slewing correction, the total uncertainty in the time difference was 200 ns. The lower timing cut (2.5 μs) and the upper time cut (20 μs) were both varied by this uncertainty in the data analysis and Monte Carlo calculation. No net systematic correction was found, but a systematic uncertainty of 2% was applied.

To sum the correlated events in the electron-photon timing peak (see Fig. 9), a window with a fixed width was applied to each series, and it encompassed nearly all of the Gaussian timing peak in the data. The variation in the peak width and coarse data binning yielded no systematic correction. It is possible, given the coarse binning and large background, that the window can be shifted. There could also be a systematic uncertainty in the extraction of the time difference, and a nonuniformity in the background that was not accounted for. In the fit, these factors can introduce a nonstatistical uncertainty in the background subtraction. To account for these possibilities, a systematic uncertainty of 2% was applied.

D. Correlated backgrounds

Correlated backgrounds are events with a valid electron-proton trigger and a photon correlated to the trigger, but this photon does not originate from the decay. These background events are split into those from external bremsstrahlung in the SBD and those from electronic artifacts. External bremsstrahlung photons are the most problematic, because there is no simple analysis cut to remove them.

1. External bremsstrahlung

The largest total contribution to the correlated background is bremsstrahlung produced when the electron slows down in the SBD. It is not necessarily the highest rate background, but it is difficult to remove with analysis cuts. These photons are produced by electron-atom collisions, and the signature of such events is identical to that of a radiative decay event. The geometry of the apparatus dramatically reduced the probability of such photons reaching the BGO crystal. Furthermore, a shield composed of ^{6}Li glass and 2 cm of lead partially occluded a direct line of sight between the two detectors. Using a realistic spectrum of the electrons impinging into the SBD, MCNP5 calculated that 3% of the total correlated electron-proton-photon events were external bremsstrahlung events. Therefore, a -3% systematic correction was made to the branching ratio, and the uncertainty was set equal to the magnitude of the correction.

2. Electronic artifacts

There are two correlated backgrounds from electronic artifacts. These events occurred at a comparatively high rate but were effectively eliminated in the analysis because of their distinct waveform shapes. One mechanism for producing a correlated background of this type is a γ-ray cascade that can occur when a cold neutron is captured on material near the detectors and triggers the data acquisition system. When a high-energy γ ray hits the SBD, it saturates the response of the detector and generates a large-amplitude pulse with a characteristic long tail. As part of the cascade, another photon may strike the BGO and be detected along with the SBD trigger. This sequence matches the same hardware conditions as a radiative decay event and contributed to the correlated peak in the electron-photon timing spectrum.

The energies of the particles and pulse shape characteristics were so pathological, however, that they were easily identified in software. The ability to discriminate these events was checked by acquiring data for two days with the neutron beam on but the SBD high voltage off. This eliminated the possibility of registering a true electron-proton trigger but allowed all other beam-related phenomena to trigger the electronics. In a two-day run, 63 events fell within the electron-photon timing window, but after the application of the standard set of cuts, no events survived.

A second source of correlated background events was associated with the -25 kV potential applied to the SBD. Occasional high-voltage discharges bled off electrons into the vacuum where they generated low-energy x rays. The waveform signatures of these events are similar to those generated in the beam-related background. The rejection efficiency of the analysis was tested by running the apparatus for almost 8 days when the reactor was off. During that time, only 17 events fell within the electron-photon timing window, and one event survived the software cuts. Assuming that one event occurs every 8 days, then 11 false events are expected in the cut data. Given that the data set contains nearly 4000 radiative decay events, this would contribute no more than 0.5% to the signal. Therefore, a -0.5% systematic correction

was required, and the applied systematic uncertainty was the magnitude of the correction.

E. Model uncertainties

Examining some of the systematic effects in the analysis is straightforward, but understanding other effects required equipment manipulation, which is not possible to accomplish during experiment runs. The Monte Carlo simulation reproduces the observed behavior in benchmarking tests, and it can used to calculate the systematic uncertainties of these effects. It is well-suited to modeling the detector registration with respect to the electromagnetic fields, the leakage of bias from the APD, and backscatter effects.

1. Registration uncertainties

The uncertainty of the photon detector placement with respect to the electromagnetic fields was analyzed by shifting the electromagnetic fields in the Monte Carlo and calculating the change in the branching ratio. The uncertainty of the photon detector placement with respect to the field coils and the electrostatic mirror was no more than 1 mm in any direction. The maximum deviation in the branching ratio was 1% from shifting the electrostatic mirror field and 2% from shifting the magnetic field. The uncertainty of the absolute field strengths arising from current or voltage uncertainties was negligible.

The placement and distribution of the neutron beam were also analyzed with the Monte Carlo. An image of the neutron beam profile was made downstream of the main decay region. This was done by irradiating a dysprosium foil with the neutron beam and exposing a photographic plate to the resulting radioactivity. The $R_{ep\gamma}/R_{ep}$ ratio versus mirror voltage was calculated with various modifications to the simulated neutron beam. At the extremes, the measured profile with no beam divergence was tested, and a uniform profile with both diverging and nondiverging beams was also tested. Beam alignment was tested with a total variation of 1 mm in all directions around the center of the photon detector. The total systematic uncertainty due to the beam profile, divergence, and alignment was estimated to be 3%.

2. APD bias leakage

Electrostatic fields due to the nearly 1400 V bias on the APD can leak into the decay region and affect the proton trajectories. At the center of the neutron beam, the maximum potential from the APD is approximately 12 V. These electrostatics results were calculated given the geometry of the apparatus and a model of the silicon APD. The APD field has a non-negligible effect when the electrostatic mirror is unbiased, but the APD field is dominated by the mirror otherwise. The Monte Carlo calculated an increase of 10% in the $R_{ep\gamma}/R_{ep}$ ratio at 0 V mirror voltage by including this field correction and a negligible change in the ratio at all other voltages. The extracted branching ratio does not change appreciably, and the systematic uncertainty was estimated to be no more than 1%. While the change of the ratio at 0 V mirror voltage did not affect the branching ratio significantly, the fit to the data was improved. By including this APD correction, the χ^2 per degree of freedom for the fit was 12.9/7 versus 17.4/7 without the correction. This corresponds to a change in the χ^2 probability of 1.5% without the correction to 7.5% with the correction.

3. Electron backscattering

The electron backscattering fraction from a SBD depends upon the incident electron energy and is very sensitive to the angle of incidence when striking the SBD. The backscatter fraction as a function of incident angle and energy was calculated in MCNP5 and Penelope [44]. These results are consistent with each other at less than 0.5% precision. As a cross-check to these simulations, a phenomenological model was also used to parametrize electron backscattering which was derived from electron backscattering studies on plastic scintillators [45,46] and modified to match the results of Martin *et al.* [47].

Electron backscattering causes some incident electrons to deposit only a fraction of their energy into the SBD, and some electrons do not deposit enough energy to be detected at all. The electron backscattering effect required a +0.2% systematic correction to the branching ratio. The difference arises from the slight difference in the electron energy spectrum and the SBD incident angle for radiative and nonradiative decays. The total variation of the backscattering correction at each mirror voltage was 0.5%, and this value was taken as the systematic uncertainty. Electron backscattering can be a significant effect (over 15% for normally incident electrons into the SBD), and the relatively small systematic correction illustrates the utility of extracting the branching ratio from the $R_{ep\gamma}/R_{ep}$ ratio.

VI. RESULTS

A. Branching ratio and comparison to theory

The observation of radiative neutron decay is supported for many reasons. The single, large peak in the electron-photon timing spectrum indicates that correlated photons are detected (Fig. 9). The analysis cuts and the geometric separation of the detectors suppress the correlated backgrounds, which implies that the correlated photons are primarily radiative decay photons. Furthermore, the response of the experimental apparatus is understood with the Monte Carlo simulation, and the energy and timing spectra of the decay products agree with predictions. This agreement is also evident as a function of electrostatic mirror voltage, which was a free parameter of the experiment.

The branching ratio was extracted from the $R_{ep\gamma}/R_{ep}$ ratio data by a least-squares fit of the data to the Monte Carlo calculation as a function of mirror voltage. A total scaling factor to the Monte Carlo evaluation served as a single fit parameter. The branching ratio extracted from the fit was $(3.09 \pm 0.32) \times 10^{-3}$, and it is consistent with theoretical calculations that predict a branching ratio of 2.85×10^{-3} in the same energy region [48]. The total uncertainty in the

branching ratio was dominated by systematic effects which were 0.30×10^{-3}. Applying the 3.4% fit uncertainty leads to a total uncertainty in the branching ratio of 0.11×10^{-3}. The photon energy spectrum was consistent with theoretical predictions, and the shape of the Monte Carlo prediction agrees with the $R_{ep\gamma}/R_{ep}$ ratio data as a function of mirror voltage.

The QED-predicted radiative decay branch of the neutron was observed at a 10% precision. Because of the $R_{ep\gamma}/R_{ep}$ ratio method, many systematic uncertainties are largely canceled. This experiment is the first observation of radiative decay photons from neutron β decay, and it is the first measurement of its branching ratio for 15 to 340 keV photons.

B. Future work

An improved measurement of the photon spectrum below the 1% level could approach effects beyond the leading-order contribution such as the effect of recoil order terms. Furthermore, a measurement of the photon circular polarization could reveal information about the Dirac structure of the weak current [7]. The use of a polarized neutron allows the investigation of new angular correlations with photon and neutron polarization [41].

Although the current result is limited by systematic effects, none of these presents a significant obstacle to improving the precision of the experiment. A dedicated calibration regime has been shown in offline tests to reduce the largest uncertainties associated with the photon detector. These calibration routines can help us understand the full detector response to the theoretical photon spectrum.

Only a small fraction of the available solid angle was probed with a single bar of BGO. A 12-element scintillation detector has been constructed that permits a precision measurement of the photon spectrum and branching ratio at the percent level. The improved statistical precision allows more observation time to be devoted to calibrations and other systematics studies. The new detector allows a position-dependent analysis of the systematic effects. This is particularly relevant for electron bremsstrahlung from the SBD. The use of other scintillators and APDs in a direct detection scheme is being investigated [24]. A more detailed treatment of these developments is found in Refs. [41,49].

ACKNOWLEDGMENTS

We thank Susan Gardner of the University of Kentucky and Herbert Breuer of the University of Maryland for useful discussions and their interest in this work. We acknowledge the support of the National Institute of Standards and Technology, US Department of Commerce, in providing the neutron facilities used in this work. This research was made possible in part by support from the National Science Foundation and a US Department of Energy interagency agreement.

[1] M. Beck *et al.*, JETP Lett. **76**, 332 (2002).
[2] J. S. Nico *et al.*, Nature (London) **444**, 1059 (2006).
[3] Y. V. Gaponov and R. U. Khafizov, Phys. At. Nucl. **59**, 1213 (1996) [Yad. Fiz. **59** 1270 (1996)].
[4] Y. V. Gaponov and R. U. Khafizov, Phys. Lett. B **379**, 7 (1996).
[5] Y. V. Gaponov and R. U. Khafizov, Nucl. Instrum. Methods A **440**, 557 (2000).
[6] F. Glück, Phys. Rev. D **47**, 2840 (1993).
[7] V. Bernard, S. Gardner, U.-G. Meißner, and C. Zhang, Phys. Lett. B **593**, 105 (2004).
[8] V. Bernard, S. Gardner, U.-G. Meißner, and C. Zhang, Phys. Lett. B **599**, 348 (2004).
[9] J. D. Jackson, *Classical Electrodynamics*, 3rd ed. (Wiley, New York, 1998).
[10] A. Czarnecki, W. J. Marciano, and A. Sirlin, Phys. Rev. D **70**, 093006 (2004).
[11] C. Amsler *et al.*, Phys. Lett. B **667**, 1 (2008).
[12] W. J. Marciano and A. Sirlin, Phys. Rev. Lett. **96**, 032002 (2006).
[13] H. Abele, Prog. Part. Nucl. Phys. **60**, 1 (2008).
[14] D. R. Yennie, S. C. Frautschi, and H. Suura, Ann. Phys. (NY) **13**, 309 (1961).
[15] J. M. Jauch and F. Rohrlich, *The Theory of Photons and Electrons* (Addison-Wesley, Reading, MA, 1955).
[16] T. Kinoshita, J. Math. Phys. **3**, 650 (1962).
[17] T. D. Lee and M. Nauenberg, Phys. Rev. B **133**, 1549 (1964).
[18] J. S. Nico, M. Arif, M. S. Dewey, T. R. Gentile, D. M. Gilliam, P. R. Huffman, D. L. Jacobson, and A. K. Thompson, J. Res. Natl. Inst. Stand. Technol. **110**, 137 (2005).
[19] H. Mumm *et al.*, Rev. Sci. Instrum. **75**, 5343 (2004).
[20] M. S. Dewey *et al.*, Phys. Rev. Lett. **91**, 152302 (2003).
[21] J. S. Nico *et al.*, Phys. Rev. C **71**, 055502 (2005).
[22] J. Byrne *et al.*, J. Phys. G **28**, 1325 (2002).
[23] B. M. Fisher *et al.*, J. Res. Natl. Inst. Stand. Technol. **110**, 421 (2005).
[24] T. R. Gentile *et al.*, Nucl. Instrum. Methods A **579**, 447 (2007).
[25] M. Boucher *et al.*, Nucl. Instrum. Methods A **505**, 136 (2003).
[26] M. Moszyński, M. Szawlowski, M. Kapusta, and M. Balcerzyk, Nucl. Instrum. Methods A **485**, 504 (2003).
[27] L. Yang *et al.*, Nucl. Instrum. Methods A **508**, 388 (2003).
[28] H. V. Piltingsrud, J. Nucl. Med. **20**, 1279 (1979).
[29] C. Amsler *et al.*, Nucl. Instrum. Methods A **480**, 494 (2002).
[30] S. Derenzo, M. Weber, E. Bourret-Courchesne, and M. Klintenberg, Nucl. Instrum. Methods A **505**, 111 (2003).
[31] Rexon Components, Inc., 24500 Highpoint Rd., Beachwood, OH 44122.
[32] Certain trade names and company products are mentioned in the text or identified in illustrations in order to adequately specify the experimental procedure and equipment used. In no case does such identification imply recommendation or endorsement by the National Institute of Standards and Technology, nor does it imply that the products are necessarily the best available for the purpose.
[33] Radiation Monitoring Devices, Inc., 44 Hunt Street, Watertown, MA 02472.
[34] M. Moszyński, M. Szawlowski, M. Kapusta, and M. Balcerzyk, Nucl. Instrum. Methods A **497**, 226 (2003).
[35] Canberra Model 2006 Proportional Counter Preamplifier, Canberra Industries, 800 Research Parkway, Meriden, CT 06450.
[36] Gage CompuScope 82G, DynamicSignals LLC, 900 N. State St., Lockport, IL 60441.

[37] M. Bhattacharya and E. Adelberger (unpublished).
[38] F. B. Brown *et al.*, A General Monte Carlo N-Particle Transport Code, Version 5 LA-UR-03-1987, 2003.
[39] J. D. Jackson, S. B. Treiman, and H. W. Wyld Jr., Phys. Rev. **106**, 517 (1957).
[40] P. Bevington and D. Robinson, *Data Reduction and Error Analysis for the Physical Sciences* (McGraw-Hill, New York, 1992).
[41] R. Cooper, Ph.D. thesis, University of Michigan, 2008.
[42] G. F. Knoll, *Radiation Detection and Measurement* (Wiley, New York, 2000).
[43] J. Zeigler and J. Manoyan, Nucl. Instrum. Methods B **35**, 215 (1998).
[44] J. Sempau, J. Fernandez-Varea, E. Acosta, and F. Salvat, Nucl. Instrum. Methods B **132**, 377 (1997).
[45] F. Wietfeldt *et al.*, Nucl. Instrum. Methods A **538**, 574 (2005).
[46] T. Tabata, R. Ito, and S. Okabe, Nucl. Instrum. Methods **94**, 509 (1971).
[47] J. Martin *et al.*, Phys. Rev. C **73**, 015501 (2006).
[48] S. Gardner (private communication).
[49] R. L. Cooper *et al.*, Nucl. Instrum. Methods A **611**, 219 (2009).